Magnetoelectronic properties of bilayer Bernal graphene

Y. H. Lai,[1] J. H. Ho,[1] C. P. Chang,[2] and M. F. Lin[1,*]
[1]*Department of Physics, National Cheng Kung University, Tainan 70101, Taiwan*
[2]*Center for General Education, Tainan University of Technology, Tainan 71002, Taiwan*
(Received 19 November 2007; published 25 February 2008)

The Peierls Hamiltonian band matrix is developed to investigate magnetoelectronic properties of bilayer Bernal graphene. A uniform perpendicular magnetic field creates many dispersionless Landau levels (LLs) at low and high energies and some oscillatory LLs at moderate energy. State degeneracy of the low LLs is two times as much as that of the high LLs. Wave functions and state energies are dominated by the interlayer atomic interactions and field strength (B_0). The former induce two groups of LLs, more low LLs, the asymmetric energy spectrum about the Fermi level, and the change of level spacing. Two sets of effective quantum numbers, n_1^{eff}'s and n_2^{eff}'s, are required to characterize all the wave functions. They are determined by the strongest oscillation modes of the dominant carrier densities; furthermore, they rely on the specific interlayer atomic hoppings. The dependence of the quite low Landau-level energies on B_0 and n_1^{eff} is approximately linear. An energy gap is produced by the magnetic field and interlayer atomic hoppings. E_g grows with increasing field strength, while it is reduced by the Zeeman effect. The main features of magnetoelectronic structures are directly reflected in the density of states. The predicted electronic properties could be verified by the experimental measurements on absorption spectra and transport properties.

DOI: 10.1103/PhysRevB.77.085426 PACS number(s): 73.20.At, 73.22.−f, 81.05.Uw

I. INTRODUCTION

Bulk graphite is one of the most extensively studied materials in both experimental[1–5] and theoretical[6–11] aspects. In general, the hexagonal graphite layers are periodically stacked in the *AB* sequence [the Bernal form, Fig. 1(a)].[1] Bulk graphite is an exotic semimetal, mainly owing to the hexagonal symmetry and the weak interlayer van der Waals interactions. Recently, the stable few-layer graphenes (monolayer, bilayer, and trilayer) have been produced by mechanical friction[12,13] and by thermal decomposition.[14,15] Such systems are very suitable for studying two-dimensional physical phenomena. They have aroused a lot of researches, e.g., band structures,[16–31] transport properties,[32–39] optical spectra,[40–45] and Coulomb excitations.[46–54] Monolayer and bilayer graphenes are, respectively, identified to display room-temperature[33] and unconventional quantum Hall effects.[34] This work is focused on the magnetoelectronic properties of a bilayer Bernal graphene in a uniform perpendicular magnetic field ($\mathbf{B}=B_0\hat{z}$). The main characteristics of the Landau levels (LLs) are investigated in detail. Comparison with previous theoretical studies is also made.

The geometric symmetry configurations have a huge influence on the electronic properties of few-layer graphenes. The honeycomb structure causes a monolayer graphene to exhibit two linear bands intersecting at the Fermi level $E_F=0$ [Fig. 1(b)]. A monolayer graphene is a zero-gap semiconductor, and its low-energy bands could be described by the fermion Dirac equation.[16] The *AB* stacking sequence in bilayer graphene induces the interlayer atomic interactions and, thus, drastically modifies the low-energy bands. There exist two pairs of parabolic conduction and valence bands [Fig. 1(c)]. Furthermore, the lowest conduction band and the highest valence band have a weak overlap near the corners of the first Brillouin zone [Fig. 1(e)]. An *AB*-stacked bilayer graphene is a semimetal with a low free carrier density. A perpendicular electric field could be applied for the modulation of the electronic properties, such as the (anti)crossing subbands, increasing band-edge states, changing subband spacing, and producing energy gap.[18] That energy gap varies from zero to a finite value corresponds to the semimetal-semiconductor transition.

Magnetoelectronic structures of monolayer and bilayer graphenes at quite low energy ($\lesssim$0.1 eV) have been theoretically studied by the effective-mass approximation[7,25,26] and the tight-binding model.[27,28] A uniform perpendicular magnetic field makes electronic states flock together and induce many LLs. For a single-layer graphene, the Landau-level energies near $E_F=0$ can be described by a simple square-root form $E_n \propto \sqrt{|n|B_0}$ (n the integer quantum number and B_0 the field strength).[7,16] The dependence on B_0 has been confirmed by the magneto-optical experiments of cyclotron resonance.[42] The interlayer atomic interactions in a bilayer Bernal graphene lead to more complicated LLs. When some interlayer atomic interactions are neglected, energies of the very low LLs are predicted to be approximately proportional to $\sqrt{n(n-1)}B_0$ ($n \geq 2$).[25,26] Their wave functions are roughly given within the effective-mass approximation. Another theoretical study utilized the Peierls tight-binding model and the interlayer hopping integrals of multiwalled carbon nanotubes to evaluate the Hofstadter-like butterfly spectra.[27] However, the minimal magnetic field ($B_0 \sim 300$ T) in the calculations is too large compared with the maximum experimental value ($\sim$50 T). A different strategy will be developed with more efficiency to diagonalize a very large Hamiltonian matrix at $B_0=1-10$ T. Effects of the interlayer atomic interactions on state energies and wave functions can be thoroughly investigated. Moreover, the LLs at moderate and high energies are also discussed.

We use the Peierls tight-binding model to research the LLs in a bilayer Bernal graphene. The bandlike Hamiltonian

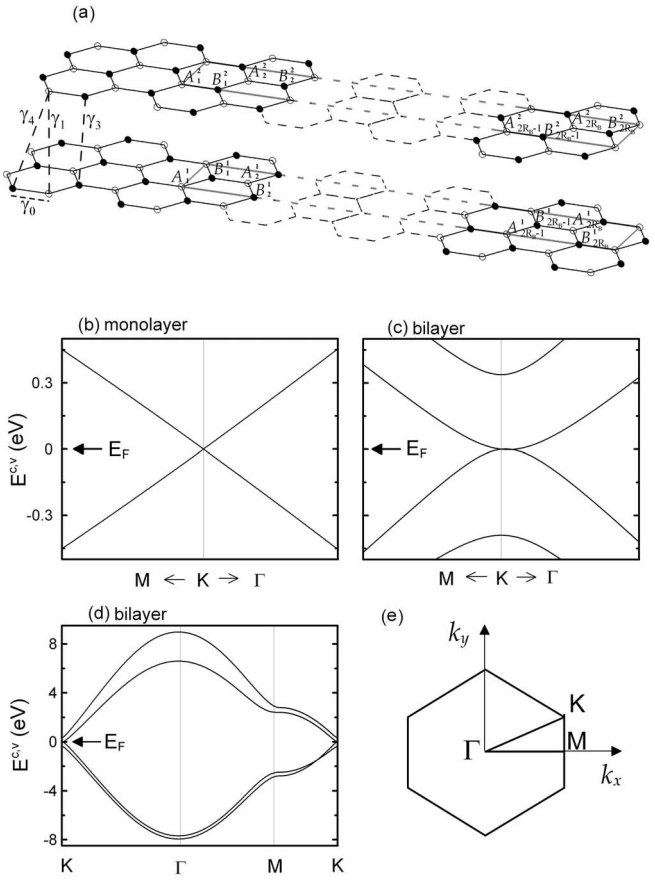

FIG. 1. (a) The geometric structure of a bilayer Bernal graphene. The primitive unit cell in a perpendicular uniform magnetic field (B_0) corresponds to the enclosed rectangles. γ_i's are the atom-atom interactions. The low-energy bands of the (b) monolayer and (c) bilayer graphenes at $B_0=0$. (d) The full π-electronic structure of a bilayer system. (e) The first Brillouin zone with the special symmetry points.

matrix, which owns the nonvanishing elements that only locate near the diagonal line, can be obtained by choosing the proper base functions. It is quite efficient in calculating state energy, wave function, energy gap, and density of states (DOS). For example, a $64\,000\times64\,000$ Hamiltonian band matrix at $B_0=10$ T can be quickly diagonalized to get the LLs. The electronic properties are primarily determined by the interlayer atomic interactions and the field strength. This work shows that they produce two groups of LLs, cause more low LLs, alter the Landau-level spacing, induce the asymmetric LLs about $E_F=0$, and open an energy gap. As for all the LLs, their quantum numbers, relationship with the specific interlayer interactions, and dependence on energy are analyzed in detail. The Zeeman splitting only reduces the field-strength-dependent energy gap for a bilayer Bernal graphene, while it creates an energy gap for a monolayer graphene.

This paper is organized as follows. In Sec. II, the Peierls tight-binding model is used to calculate the π-electronic structure. The Hamiltonian band matrix is derived for a bilayer Bernal graphene in a uniform perpendicular magnetic field. Magnetoelectronic properties, state energy, wave function, energy gap, and density of states are discussed in Sec. III. The present results are compared with previous studies. Concluding remarks are given in Sec. IV.

II. PEIERLS TIGHT-BINDING MODEL

The geometric structure of an *AB*-stacked bilayer graphene is shown in Fig. 1(a). The interlayer distance is $d=3.35$ Å and the C-C bond length is $b'=1.42$ Å. One layer could be obtained by shifting another layer along the armchair direction (the x axis) with b'. *A* atoms on the two layers have the same (x,y) coordinates, while *B* atoms are projected at the hexagonal centers of the adjacent layer. There are four kinds of atom-atom interactions in the calculations.[9] $\gamma_0=2.598$ eV, $\gamma_1=0.364$ eV, $\gamma_3=0.319$ eV, and $\gamma_4=0.177$ eV are the atomic hopping integrals, respectively, from two nearest-neighbor atoms on the same layer, between A^1 and A^2 atoms, between B^1 and B^2 atoms, and between A^1 and B^2 atoms (A^2 and B^1 atoms). The superscripts 1 and 2 represent the first and second layers. Since the nearest-neighbor atoms have different chemical environments, the difference in the site energy is characterized by $\gamma_6=-0.026$ eV. The interlayer atomic interactions γ_3 and γ_4 are neglected in Refs. 25 and 26, and site energy γ_6 is absent in Refs. 25–27.

The Hamiltonian without an external field is $H=(p^2/2m)+V(\mathbf{r})$. There are four carbon atoms in a primitive unit cell. The tight-binding Bloch function could be expressed as

$$|\Psi_{\mathbf{k}}\rangle = f_1|A_{\mathbf{k}}^1\rangle + f_2|B_{\mathbf{k}}^1\rangle + f_3|A_{\mathbf{k}}^2\rangle + f_4|B_{\mathbf{k}}^2\rangle, \tag{1}$$

where $|A_{\mathbf{k}}^1\rangle$ ($|B_{\mathbf{k}}^1\rangle$, $|A_{\mathbf{k}}^2\rangle$; $|B_{\mathbf{k}}^2\rangle$) is the linear superposition of the $2p_z$ orbitals from the periodic A^1 (B^1, A^2; B^2) atoms. The Hamiltonian built from the four tight-binding functions is a 4×4 Hermitian matrix. The independent nonvanishing matrix elements are

$$\langle B_{\mathbf{k}}^1|H|A_{\mathbf{k}}^1\rangle = \langle A_{\mathbf{k}}^2|H|B_{\mathbf{k}}^2\rangle \approx \gamma_0 \sum_{nn} \frac{1}{N} \exp[i\mathbf{k}\cdot(\mathbf{R}_{A^1}-\mathbf{R}_{B^1})] \equiv \gamma_0 t, \tag{2}$$

$$\langle A_{\mathbf{k}}^2|H|A_{\mathbf{k}}^1\rangle \approx \gamma_1, \tag{3}$$

$$\langle B_{\mathbf{k}}^2|H|B_{\mathbf{k}}^1\rangle \approx \gamma_3 t, \tag{4}$$

$$\langle B_{\mathbf{k}}^1|H|A_{\mathbf{k}}^2\rangle = \langle A_{\mathbf{k}}^1|H|B_{\mathbf{k}}^2\rangle \approx \gamma_4 t, \tag{5}$$

$$\langle A_{\mathbf{k}}^1|H|A_{\mathbf{k}}^1\rangle = \langle A_{\mathbf{k}}^2|H|A_{\mathbf{k}}^2\rangle \approx \gamma_6. \tag{6}$$

The summation in Eq. (2) only takes into account the nearest-neighbor atoms at $\mathbf{R}_{A^1}$ and $\mathbf{R}_{B^1}$. $t=2\cos\times(\sqrt{3}b'k_y/2)\exp(-ib'k_x/2)+\exp(ib'k_x)$ is the summation of the phase terms due to three nearest-neighbor interactions.

The bilayer Bernal graphene is present in a uniform perpendicular magnetic field $\mathbf{B}=B_0\hat{z}$. The Hamiltonian becomes $H_B=[(p-e\mathbf{A}/c)^2/2m]+V(\mathbf{r})$, and $\mathbf{B}$ will induce the Peierls phase characterized by the vector potential $\mathbf{A}=B_0x\hat{y}$ [Eq. (7)]. The magnetic flux through a hexagon in the unit of a flux quantum ($\Phi_0=hc/e$) is $\Phi=3\sqrt{3}B_0b'^2/2\Phi_0$. Its inverse is assumed to be a positive integer, i.e., $1/\Phi=R_B$. The magnetic field makes the Peierls phases exhibit the periodical oscillations along the x axis. Such phases have a period $2/\Phi=2R_B$; therefore, the enlarged primitive unit cell is a rectangle with $8R_B$ carbon atoms [Fig. 1(a)]. To obtain the Hamiltonian band matrix, the base functions are arranged in the specific sequence $\{|A^1_{1\mathbf{k}}\rangle,|A^2_{1\mathbf{k}}\rangle,|B^2_{2R_B\mathbf{k}}\rangle,|B^1_{2R_B\mathbf{k}}\rangle,\times|B^1_{1\mathbf{k}}\rangle,|B^2_{1\mathbf{k}}\rangle,|A^2_{2R_B\mathbf{k}}\rangle,|A^1_{2R_B\mathbf{k}}\rangle,\ldots,|A^1_{R_B-1\mathbf{k}}\rangle,|A^2_{R_b-1\mathbf{k}}\rangle,|B^2_{R_B\mathbf{k}}\rangle,\times|B^1_{R_B\mathbf{k}}\rangle,|B^1_{R_B-1\mathbf{k}}\rangle,|B^2_{R_B-1\mathbf{k}}\rangle,|A^2_{R_B\mathbf{k}}\rangle;|A^1_{R_B\mathbf{k}}\rangle\}$. The dominant Hamiltonian matrix elements include

$$\langle B^1_{j'\mathbf{k}}|H_\mathbf{B}|A^1_{i'\mathbf{k}}\rangle \approx \gamma_0\sum_{nn}\frac{1}{N}\exp[i\mathbf{k}\cdot(\mathbf{R}_{A^1_{i'}}-\mathbf{R}_{B^1_{j'}})]\times\exp\left\{i\left[\frac{2\pi}{\Phi_0}\int_{\mathbf{R}_{A^1_{i'}}}^{\mathbf{R}_{B^1_{j'}}}\mathbf{A}\cdot d\mathbf{r}\right]\right\} \equiv \gamma_0 t_{1,i'}\delta_{i',j'}+\gamma_0 q\delta_{i',j'+1}, \tag{7}$$

$$\langle B^1_{j'\mathbf{k}}|H_\mathbf{B}|A^2_{i'\mathbf{k}}\rangle \approx \gamma_4 t_{1,i'}\delta_{i',j'}+\gamma_4 q\delta_{i',j'+1}, \tag{8}$$

$$\langle A^2_{j'\mathbf{k}}|H_\mathbf{B}|A^1_{i'\mathbf{k}}\rangle \approx \gamma_1\delta_{i',j'}, \tag{9}$$

$$\langle B^2_{j'\mathbf{k}}|H_\mathbf{B}|B^1_{i'\mathbf{k}}\rangle \approx \gamma_3 t_{2,i'}\delta_{i',j'}+\gamma_3 q\delta_{i',j'+1}, \tag{10}$$

$$\langle A^2_{j'\mathbf{k}}|H_\mathbf{B}|B^2_{i'\mathbf{k}}\rangle \approx \gamma_0 t_{3,i'}\delta_{i',j'-1}+\gamma_0 q\delta_{i',j'}, \tag{11}$$

$$\langle A^1_{j'\mathbf{k}}|H_\mathbf{B}|B^2_{i'\mathbf{k}}\rangle \approx \gamma_4 t_{3,i'}\delta_{i',j'-1}+\gamma_4 q\delta_{i',j'}, \tag{12}$$

$$\langle A^1_{j'\mathbf{k}}|H_\mathbf{B}|A^1_{i'\mathbf{k}}\rangle = \langle A^2_{j'\mathbf{k}}|H_\mathbf{B}|A^2_{i'\mathbf{k}}\rangle = \gamma_6\delta_{i',j'}, \tag{13}$$

$$\langle B^1_{j'\mathbf{k}}|H_\mathbf{B}|B^1_{i'\mathbf{k}}\rangle = \langle B^2_{j'\mathbf{k}}|H_\mathbf{B}|B^2_{i'\mathbf{k}}\rangle = 0. \tag{14}$$

The integration in Eq. (7) is the extra position-dependent Peierls phase on the hopping integral. The four independent phase terms are

$$t_{1,i'}=\exp\{i[-(k_xb'/2)-(\sqrt{3}k_yb'/2)+\pi\Phi(i'-1)+(1/6)]\}+\exp\{i[-(k_xb'/2)+(\sqrt{3}k_yb'/2)-\pi\Phi(i'-1)+(1/6)]\},$$
$$t_{2,i'}=\exp\{i[-(k_xb'/2)-(\sqrt{3}k_yb'/2)+\pi\Phi(i'-1)+(3/6)]\}+\exp\{i[-(k_xb'/2)+(\sqrt{3}k_yb'/2)-\pi\Phi(i'-1)+(3/6)]\},$$
$$t_{3,i'}=\exp\{i[-(k_xb'/2)-(\sqrt{3}k_yb'/2)+\pi\Phi(i'-1)+(5/6)]\}+\exp\{i[-(k_xb'/2)+(\sqrt{3}k_yb'/2)-\pi\Phi(i'-1)+(5/6)]\},$$

and

$$q=\exp[i(-k_yb')].$$

After the detailed calculations, the $8R_B\times 8R_B$ Hermitian Hamiltonian band matrix is given by

$$\begin{pmatrix} H_1 & H_{a,i'=1} & 0 & 0 & \cdots & 0 \\ H^\dagger_{a,i'=1} & H_{s,i'=1} & H_{a,i'=2} & 0 & \cdots & 0 \\ 0 & H^\dagger_{a,i'=2} & H_{s,i'=2} & H_{a,i'=3} & \ddots & 0 \\ 0 & 0 & H^\dagger_{a,i'=3} & H_{s,i'=3} & \ddots & 0 \\ \vdots & \vdots & \ddots & \ddots & \ddots & H_{a,i'=R_B-1} \\ 0 & 0 & 0 & 0 & H^\dagger_{a,i'=R_B-1} & H_{R_B} \end{pmatrix}, \tag{15}$$

where the four independent

8×8 block matrices are expressed

$$H_1=\begin{pmatrix} \gamma_6 & \gamma_1 & \gamma_4 t_{2,2R_B} & \gamma_0 q^* & \gamma_0 t^*_{1,1} & \gamma_4 q & 0 & 0 \\ \gamma_1 & \gamma_6 & \gamma_0 t_{2,2R_B} & \gamma_4 q^* & \gamma_4 t^*_{1,1} & \gamma_0 q & 0 & 0 \\ \gamma_4 t^*_{2,2R_B} & \gamma_0 t^*_{2,2R_B} & 0 & \gamma_3 t^*_{3,2R_B} & \gamma_3 q & 0 & \gamma_0 q^* & \gamma_4 q^* \\ \gamma_0 q & \gamma_4 q & \gamma_3 t_{3,2R_B} & 0 & 0 & 0 & \gamma_4 t_{1,2R_B} & \gamma_0 t_{1,2R_B} \\ \gamma_0 t_{1,1} & \gamma_4 t_{1,1} & \gamma_3 q^* & 0 & 0 & \gamma_3 t_{3,1} & 0 & 0 \\ \gamma_4 q^* & \gamma_0 q^* & 0 & 0 & \gamma_3 t^*_{3,1} & 0 & 0 & 0 \\ 0 & 0 & \gamma_0 q & \gamma_4 t^*_{1,2R_B} & 0 & 0 & \gamma_6 & \gamma_1 \\ 0 & 0 & \gamma_4 q & \gamma_0 t^*_{1,2R_B} & 0 & 0 & \gamma_1 & \gamma_6 \end{pmatrix},$$

$$H_{R_B} = \begin{pmatrix} \gamma_6 & \gamma_1 & 0 & 0 & \gamma_0 t^*_{1,R_B} & \gamma_4 q & 0 & 0 \\ \gamma_1 & \gamma_6 & 0 & 0 & \gamma_4 t^*_{1,R_B} & \gamma_0 q & 0 & 0 \\ 0 & 0 & 0 & \gamma_3 t^*_{3,R_B} & 0 & 0 & \gamma_0 q^* & \gamma_4 q^* \\ 0 & 0 & \gamma_3 t_{3,R_B} & 0 & 0 & \gamma_3 q_* & \gamma_4 t_{1,R_B+1} & \gamma_0 t_{1,R_B+1} \\ \gamma_0 t_{1,R_B} & \gamma_4 t_{1,R_B} & 0 & 0 & 0 & \gamma_3 t_{3,R_B} & \gamma_4 q & -\gamma_0 q \\ \gamma_4 q^* & \gamma_0 q^* & 0 & \gamma_3 q & \gamma_3 t^*_{3,R_B} & 0 & \gamma_0 t^*_{2,R_B} & \gamma_4 t^*_{2,R_B} \\ 0 & 0 & \gamma_0 q & \gamma_4 t^*_{1,R_B+1} & \gamma_4 q^* & \gamma_0 t_{2,R_B} & \gamma_6 & \gamma_1 \\ 0 & 0 & \gamma_4 q & \gamma_0 t^*_{1,R_B+1} & \gamma_0 q^* & \gamma_4 t_{2,R_B} & \gamma_1 & \gamma_6 \end{pmatrix},$$

$$H_{a,i'} = \begin{pmatrix} 0 & 0 & 0 & 0 & 0 & 0 & 0 & 0 \\ 0 & 0 & 0 & 0 & 0 & 0 & 0 & 0 \\ 0 & 0 & 0 & 0 & 0 & 0 & 0 & 0 \\ 0 & 0 & \gamma_3 q^* & 0 & 0 & 0 & 0 & 0 \\ \gamma_0 q & \gamma_4 q & 0 & 0 & 0 & 0 & 0 & 0 \\ \gamma_4 t^*_{1,i'} & \gamma_0 t^*_{1,i'} & 0 & 0 & \gamma_3 q & 0 & 0 & 0 \\ 0 & 0 & \gamma_0 t_{1,2R_B-i'} & \gamma_4 q^* & 0 & 0 & 0 & 0 \\ 0 & 0 & \gamma_4 t_{1,2R_B-i'} & \gamma_0 q^* & 0 & 0 & 0 & 0 \end{pmatrix},$$

$$H_{s,i'} = \begin{pmatrix} \gamma_6 & \gamma_1 & 0 & 0 & \gamma_0 t^*_{1,i'+1} & \gamma_4 q & 0 & 0 \\ \gamma_1 & \gamma_6 & 0 & 0 & \gamma_4 t^*_{1,i'+1} & \gamma_0 q & 0 & 0 \\ 0 & 0 & 0 & \gamma_3 t^*_{3,2R_B-i'} & 0 & 0 & \gamma_0 q^* & \gamma_4 q^* \\ 0 & 0 & \gamma_3 t_{3,2R_B-i'} & 0 & 0 & \gamma_3 q_* & \gamma_4 t_{1,2R_B-i'} & \gamma_0 t_{1,2R_B-i'} \\ \gamma_0 t_{1,i'+1} & \gamma_4 t_{1,i'+1} & 0 & 0 & 0 & \gamma_3 t_{3,i'+1} & 0 & 0 \\ \gamma_4 q^* & \gamma_0 q^* & 0 & 0 & \gamma_3 t^*_{3,i'+1} & 0 & 0 & 0 \\ 0 & 0 & \gamma_0 q & \gamma_4 t^*_{1,2R_B-i'} & 0 & 0 & \gamma_6 & \gamma_1 \\ 0 & 0 & \gamma_4 q & \gamma_0 t^*_{1,2R_B-i'} & 0 & 0 & \gamma_1 & \gamma_6 \end{pmatrix}.$$

The Hamiltonian band matrix in Eq. (15) could be used to solve eigenvalues ($E^{c,v}$'s) and eigenfunctions ($\Psi^{c,v}$'s) efficiently even for a very small magnetic flux or a huge R_B ($R_B > 79\,000$ for $B_0 < 1$ T). They will be useful in studying other physical properties. c and v, respectively, represent the unoccupied conduction states and occupied valence states.

III. MAGNETOELECTRONIC PROPERTIES

The π-electronic structures of monolayer and bilayer Bernal graphenes without B_0 are simply reviewed. The low-energy bands of a monolayer graphene exhibit two linear dispersions intersecting at $E_F=0$ because of the hexagonal symmetry [Fig. 1(b)]. The interlayer atomic interactions in the bilayer system induce two pairs of parabolic bands and asymmetry of energy spectrum about the Fermi level [Fig. 1(c)]. The first pair near $E_F=0$ has a very weak overlap. The band-edge states of the second pair occur at $E^c \approx \gamma_1 + \gamma_6$ and $E^v \approx -\gamma_1 + \gamma_6$. Such state energies depend on the A^1-A^2 atomic interaction and site energy, but not on the B^1-B^2 and A^1-B^2 (B^1-A^2) atomic interactions. Both γ_3 and γ_4 display remarkable effects on the energy dispersions of parabolic bands (or DOS) and the band overlap. DOS of parabolic bands is higher than that of linear ones; that is, the low DOS is enhanced by the interlayer atomic interactions. The π-electronic structures at moderate and high energies are, respectively, determined by the symmetry points M and Γ, as shown in Fig. 1(d). The point M corresponds to state energies

$$E^c \approx [\sqrt{4(\gamma_0^2 - 2\gamma_0\gamma_4)} - \gamma_1 - \gamma_3 + \gamma_6]/2,$$

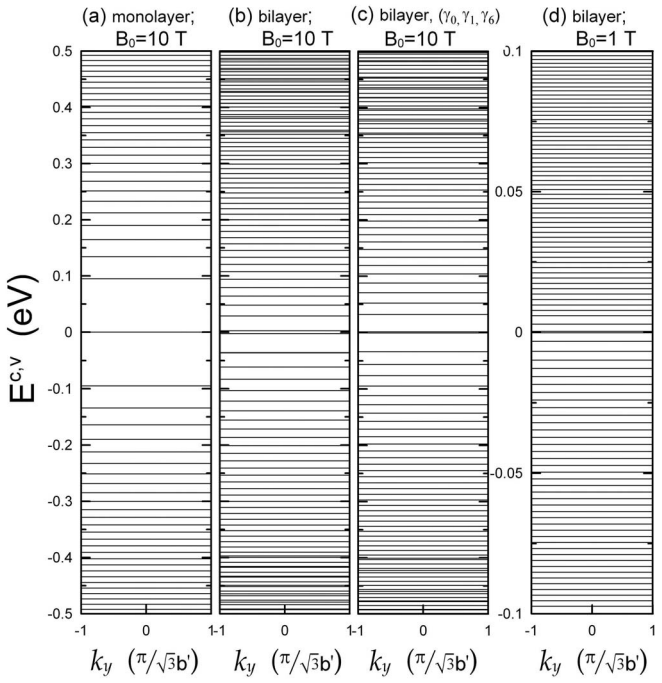

FIG. 2. The low Landau-level energies for (a) a monolayer graphene at $B_0=10$ T, (b) a bilayer graphene at $B_0=10$ T, (c) a bilayer graphene only with the specific atom-atom interactions $(\gamma_0, \gamma_1, \gamma_6)$ at $B_0=10$ T, and (d) a bilayer graphene at $B_0=1$ T.

$$E^c \approx [\sqrt{4(\gamma_0^2+2\gamma_0\gamma_4)}+\gamma_1+\gamma_3+\gamma_6]/2,$$
$$E^v \approx [-\sqrt{4(\gamma_0^2-2\gamma_0\gamma_4)}-\gamma_1-\gamma_3+\gamma_6]/2,$$

and

$$E^v \approx [-\sqrt{4(\gamma_0^2+2\gamma_0\gamma_4)}+\gamma_1+\gamma_3+\gamma_6]/2.$$

It belongs to a saddle point in the energy-wave-vector space and, thus, exhibits the highest DOS.[18] The point Γ, which is associated with the π bandwidth, has state energies

$$E^c \approx (\sqrt{36\gamma_0^2+48\gamma_0\gamma_4+12\gamma_1^2}+\gamma_1+3\gamma_3+\gamma_6)/2,$$
$$E^c \approx (\sqrt{36\gamma_0^2-48\gamma_0\gamma_4+12\gamma_1^2}-\gamma_1-3\gamma_3+\gamma_6)/2,$$
$$E^v \approx (-\sqrt{36\gamma_0^2+48\gamma_0\gamma_4+12\gamma_1^2}+\gamma_1+3\gamma_3+\gamma_6)/2,$$

and

$$E^v \approx (-\sqrt{36\gamma_0^2-48\gamma_0\gamma_4+12\gamma_1^2}-\gamma_1-3\gamma_3+\gamma_6)/2.$$

A uniform perpendicular magnetic field in a monolayer graphene creates many dispersionless LLs at low energy, as shown in Fig. 2(a). The LLs are fourfold degenerate for each $\mathbf{k}$ and symmetric about $E_F=0$. Their energies obey a simple power-law relation $E_n \propto \sqrt{|n|B_0}$.[7,16] The energy spacing (E_s) between two adjacent LLs declines quickly with the increasing Landau-level energy. The fourfold degeneracy remains unchanged in a bilayer Bernal graphene, as shown in Fig. 2(b). On the other hand, the interlayer atomic interactions could lead to the asymmetric LLs about $E_F=0$, more low LLs, two groups of LLs, the drastic change of the Landau-level spacing, and an energy gap. The higher the DOS at $B_0=0$ is, the denser LLs will be. The first three results principally come from the interlayer atomic interactions, which can be seen from the above-mentioned results at $B_0=0$. The other effects are also related to the field strength. The first group of LLs appears at $|E^{c,v}|>0$ and the second one begins

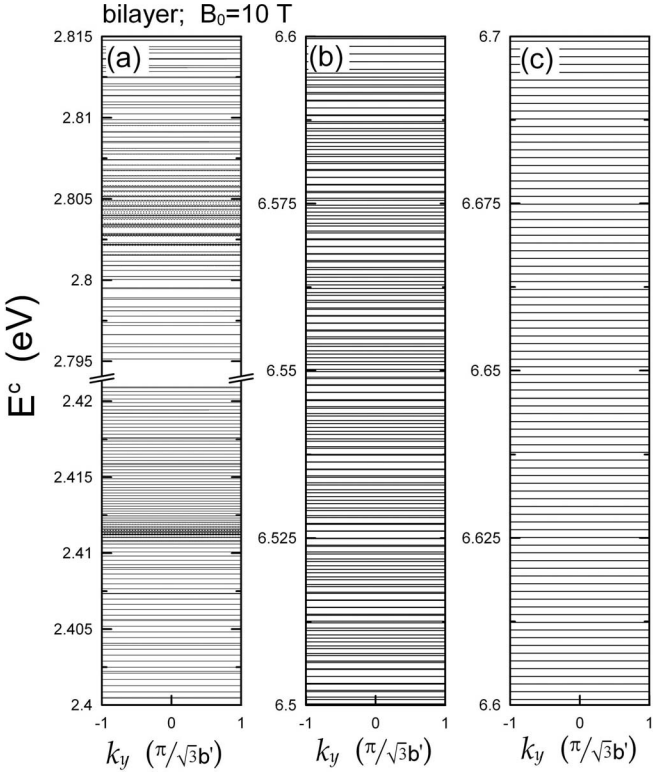

FIG. 3. The (a) moderate- and [(b) and (c)] high-energy LLs of a bilayer graphene at $B_0=10$ T.

at $E^c \gtrsim \gamma_1+\gamma_6$ and $E^v \lesssim -\gamma_1+\gamma_6$. The latter just corresponds to the second pair of parabolic bands at $B_0=0$ [Fig. 1(c)]. Apparently, the occurrence of two groups of LLs is governed by the A^1-A^2 atomic interaction and site energy. It is also accompanied by the disorder of the Landau-level spacing.

The number, state degeneracy, energy dispersion, and energy spacing of the LLs strongly rely on the energy regimes. The LLs rapidly grow as energy increases from zero. There exist the densest LLs at moderate energy $[\sqrt{4(\gamma_0^2-2\gamma_0\gamma_4)}-\gamma_1-\gamma_3+\gamma_6]/2 \lesssim E^c \lesssim [\sqrt{4(\gamma_0^2+2\gamma_0\gamma_4)}+\gamma_1+\gamma_3+\gamma_6]/2$, as shown in Fig. 3(a). This result reflects the fact that the highest DOS of a graphene system is dominated by the saddle point M. State degeneracies of the moderate LLs are mixed up within the range $[\sqrt{4(\gamma_0^2-2\gamma_0\gamma_4)}-\gamma_1-\gamma_3+\gamma_6]/2 \lesssim E^c \lesssim [\sqrt{4(\gamma_0^2+2\gamma_0\gamma_4)}+\gamma_1+\gamma_3+\gamma_6]/2$. These LLs might be doubly or fourfold degenerate. Furthermore, some of them exhibit oscillatory energy dispersions. The Landau-level density decreases with the further increase of energy [Figs. 3(b) and 3(c)]. The high LLs are twofold degenerate at $E^c \gtrsim [\sqrt{4(\gamma_0^2+2\gamma_0\gamma_4)}+\gamma_1+\gamma_3+\gamma_6]/2$. The first group of LLs vanishes at $E^c \gtrsim (\sqrt{36\gamma_0^2-48\gamma_0\gamma_4+12\gamma_1^2}-\gamma_1-3\gamma_3+\gamma_6)/2$. Only the second group of LLs survives there [Fig. 3(c)] so that the Landau-level spacing can change in order.

The effects of the interlayer atomic interactions and the field strength on the LLs deserve a closer examination. When the B^1-B^2 and A^1-B^2 (B^1-A^2) atomic interactions are neglected, the calculated results, as shown in Fig. 2(c), are almost the same with those obtained in Refs. 25 and 26. The Landau-level energy lower than 0.2 eV could be approximately characterized by a simple relation E^c

$\propto \sqrt{n_1^{eff}(n_1^{eff}-1)}B_0$ (n_1^{eff} will be defined later), and the energy gap $E_g \simeq 1.7$ meV is fairly small at $B_0=10$ T. Both γ_3 and γ_4 significantly affect the Landau-level energy and the band gap, as seen from a comparison between Figs. 2(b) and 2(c). The fact that they can alter the parabolic energy dispersion and band overlap in the $B_0=0$ case accounts for this result. More LLs take shape with decreasing field strength, as shown in Fig. 2(d) at $B_0=1$ T. Moreover, the Landau-level spacing, state degeneracy associated with k_x, and energy gap are reduced.

The main characteristics of wave functions can be proposed to define the quantum number of each LL. In a primitive unit cell, $8R_B$ carbon atoms are categorized into eight groups A_o^1, A_e^1, B_o^1, B_e^1, A_o^2, A_e^2, B_o^2, and B_e^2, where o and e are odd and even integers, respectively. The wave function is expressed as eight groups of subenvelope functions:

$$|\Psi^{c,v}\rangle = \sum_o f^{c,v}_{A^1_o}|A^1_o\rangle + \sum_e f^{c,v}_{A^1_e}|A^1_e\rangle + \sum_o f^{c,v}_{B^1_o}|B^1_o\rangle + \sum_e f^{c,v}_{B^1_e}|B^1_e\rangle + \sum_o f^{c,v}_{A^2_o}|A^2_o\rangle + \sum_e f^{c,v}_{A^2_e}|A^2_e\rangle + \sum_o f^{c,v}_{B^2_o}|B^2_o\rangle + \sum_e f^{c,v}_{B^2_e}|B^2_e\rangle. \tag{16}$$

The two LLs nearest to $E_F=0$ are the lowest unoccupied LLs (LULLs) and the highest occupied LLs (HOLLs). Their energies are $E^c=E_g/2$ and $E^v=-E_g/2$, respectively. The wave functions of the LULLs exhibit the special probability distributions in a primitive unit cell, as shown in Fig. 4(a) for $|\Psi_{LULLs}|^2$ at ($k_x=0$, $k_y=0$). Carbon atoms with odd indices and those with even indices make equal contributions to wave functions. The subenvelope functions associated with them on the same plane might have opposite amplitudes, e.g., $f^c_{A^1_o}=-f^c_{A^1_e}$ and $f^c_{B^1_o}=-f^c_{B^1_e}$. All the subenvelope functions mainly come from the $2p_z$ orbitals centering at one-sixth of a primitive unit cell ($A_N/4R_B=B_N/4R_B=1/6$; N represents the Nth A or B atom). They exhibit the oscillatory behavior. The number of zero point (n), which stands for the spatial symmetry, is chosen to characterize a subenvelope function. This quantum number depends on the graphene position and the basis atoms (the A or B atoms). For example, the probability distributions of four subenvelope functions ($|f^c_{A^1_o}|^2$, $|f^c_{B^1_o}|^2$, $|f^c_{A^2_o}|^2$, $|f^c_{B^2_o}|^2$) have the quantum numbers $n=2$, $n=1$, $n=2$, and $n=0$, respectively. Among them, the carrier density due to the B atoms on the second layer is much higher than the others; therefore, $n_1^{eff}=0$ is regarded as the effective quantum number of the LULLs. In addition, the fourfold degenerate LULLs have similar wave functions, and their differences only lie in the interchange of two graphene layers or the sign changes of the subenvelope functions. Similar results could also be found in the HOLLs, as shown in Fig. 4(b). The B atoms on the second layer, with the largest carrier density, exhibit the oscillation of one zero point. The HOLLs are, thus, defined as the $n_1^{eff}=1$ states.

The effective quantum number is identical for the m_1th unoccupied and occupied LLs away from $E_F=0$ ($m_1 \geqslant 2$), while the opposite is true for the LULLs and HOLLs. Accordingly, it is sufficient to discuss the m_1th unoccupied LLs

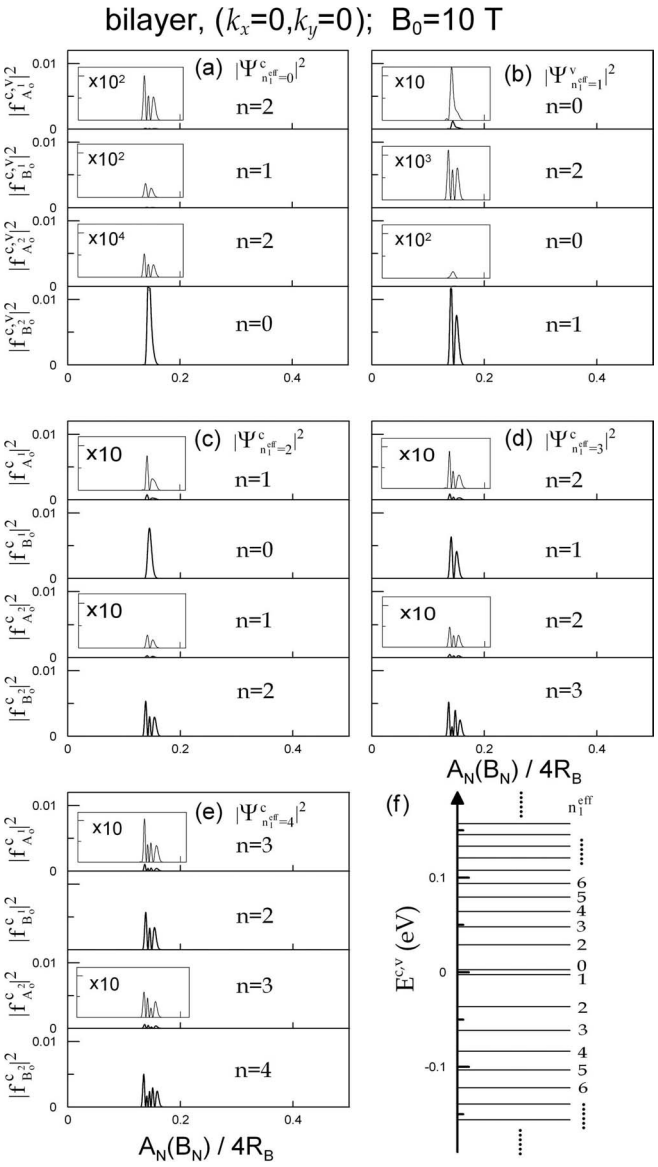

FIG. 4. The carrier densities on two graphene layers at ($k_x=0, k_y=0$) and $B_0=10$ T for (a) the lowest unoccupied LLs, (b) the highest occupied LLs, and (c) the second, (d) the third, and (e) the fourth unoccupied LLs. They are due to the A_o^1, B_o^1, A_o^2, and B_o^2 atoms. (f) The quite low Landau-level energy versus the effective quantum number n_1^{eff}.

only. The second unoccupied LLs are mainly determined by the B atoms on the first and second layers, as shown in Fig. 4(c). Their subenvelope functions, respectively, belong to the $n=0$ and $n=2$ modes. The total carrier distributions on two layers are almost the same [the approximately equal areas in Fig. 4(c)]; that is, the two modes are of equal importance. The third and fourth unoccupied LLs exhibit similar subenvelope functions, as shown in Figs. 4(d) and 4(e). The two subenvelope functions of $n=m_1-2$ and $n=m_1$ dominate the carrier distributions. n corresponding to the strongest oscillation mode is chosen as the effective quantum number. That n_1^{eff} is just equal to m_1 is very convenient in defining the other LLs [Fig. 4(f)]. Such choice might have some deficiencies, because the importance of the A atoms is gradually

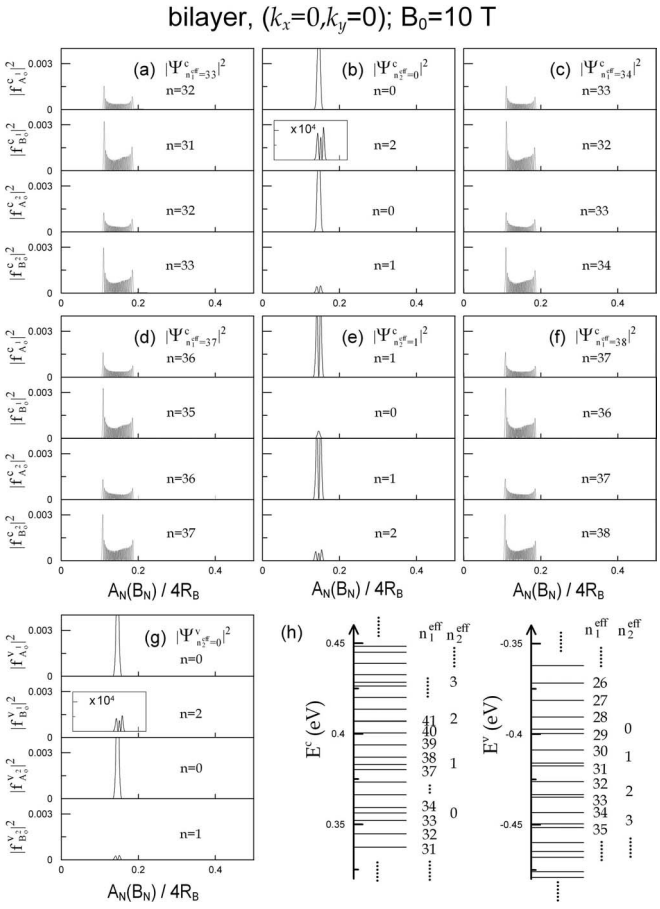

FIG. 5. Similar plot as Fig. 4, but shown at the energy range with two groups of LLs. The carrier densities for (a) the 33rd, (c) the 34th, (d) the 37th, and (f) the 38th unoccupied LLs of the first group. Those for (b) the lowest unoccupied LLs, (e) the second unoccupied LLs, and (g) the highest occupied LLs of the second group. (h) The relation between the low Landau-level energy and (n_1^{eff}, n_2^{eff}).

enhanced with the increase of energy (the following paragraph).

The interlayer atomic interactions govern the π-electronic structure at $B_0=0$ and, thus, enrich the wave functions of the LLs. When the unoccupied LLs gradually move away from $E_F=0$, the A atoms would play an important role in the carrier density. The unoccupied LLs of $m_1=33$ ($m_1=34$) have energies close to γ_1. The subenvelope functions from the A atoms exhibit the strong oscillations of $n=32$ ($n=33$) on two layers, as shown in Fig. 5(a) [Fig. 5(c)]. Their amplitudes are comparable to those from the B atoms, which is in sharp contrast with the case at energy $E^c \leqslant 0.1$ eV (Fig. 4). The contributions due to the A atoms are not negligible. However, the highest oscillation mode of the B atoms on the second layer is taken to define the effective quantum number. $n_1^{eff}=m_1$ remains unaltered at other energy regimes.

In addition to the rich subenvelope functions, the interlayer atomic hoppings also cause another group of LLs for $E^c \gtrsim \gamma_1+\gamma_6$ and $E^v \lesssim -\gamma_1+\gamma_6$, as shown in Figs. 5(b) and 5(g) for the LULLs and HOLLs, respectively. The LULLs (HOLLs) of the second group, as plotted in Fig. 5(h), locate between the unoccupied (occupied) LLs of $m_1=33$ ($m_1=28$) and $m_1=34$ ($m_1=29$). They are mostly determined by the A atoms, but not by the B atoms. The subenvelope functions of the former belong to the $n=0$ mode, and they have an equal carrier density on two layers ($|f^c_{A_1}|^2=|f^c_{A_2}|^2$; $|f^v_{A_1}|^2=|f^v_{A_2}|^2$). The effective quantum number of the LULLs (HOLLs) is $n_2^{eff}=0$, as defined earlier for the first group of LLs. These fairly similar results are obtained for the LULLs and HOLLs of the second group, e.g., $n_2^{eff}=0$ and the dominant contribution of the A atoms. However, for the LULLs and HOLLs of the first group, the effective quantum number is different ($n_1^{eff}=0$ and $n_1^{eff}=1$ for the LULLs and HOLLs, respectively), and the main contribution is due to the B atoms on the second layer. The weak overlap between the very low valence and conduction bands at $B_0=0$ [Fig. 1(c)] might be responsible for the important differences between two groups of LLs. That the A atoms on two layers dominate the carrier distribution keeps being unchanged with the increase of energy, e.g., the second unoccupied LLs shown at Fig. 5(e). Their oscillation modes are employed to characterize the effective quantum number n_2^{eff}. The second unoccupied LLs, which are between $m_1=37$ and $m_1=38$ [Figs. 5(d) and 5(f)], have $n_2^{eff}=1$. The effective quantum numbers of the other unoccupied LLs are given by $n_2^{eff}=2,3,4,\ldots$. The occupied LLs exhibit the same n_2^{eff}'s [Fig. 5(h)]. In short, two sets of effective quantum number are required to characterize all the wave functions. They depend on the specific interlayer atomic interactions. (n_1^{eff}, n_2^{eff}) represent the spatial symmetry configurations; therefore, they are expected to satisfy the special selection rule during the excitation processes.

The pretty low LLs of the first group deserve a closer investigation on the n_1^{eff} and B_0 dependence. The dependence of the Landau-level energy on n_1^{eff}, as shown in Fig. 6(a), is approximately linear at the energy regime $|E^{c,v}| \lesssim 50$ meV. There are sufficient LLs ($\gtrsim$50 LLs; solid circles) to observe such dependence when the magnetic field is smaller than 1 T. It is noted that the very low Landau-level energies can also be approximated by $|E^{c,v}| \propto [n_1^{eff}(n_1^{eff}-1)]^{1/2}$ [inset in Fig. 6(a) at $B_0=0.5$ T].[25,26] Two kinds of n_1^{eff} dependence are supported by the transport measurements on the surface of the bulk graphite.[5] On the other hand, at $|E^{c,v}| \gtrsim 50$ meV, the nonlinear behavior is highlighted by the gradual decrease of the Landau-level spacing. Concerning the magnetic-field dependence, $|E^{c,v}| \lesssim 50$ meV is also suitable for the identification of the linear behavior, as shown in Fig. 6(b). The B_0 dependence is getting weak at another energy regime. From the second LLs of $n_1^{eff}=2$ (open circles), the maximal magnetic field applied to test the linear dependence is deduced to be about 20 T. The first unoccupied and occupied LLs dominate the energy gap; that is, $E_g=E^c(n_1^{eff}=1)-E^v(n_1^{eff}=0)$. Energy gap grows with increasing field strength [open squares in Fig. 6(c)]. However, a monolayer graphene has $E_g=0$ for any magnetic field.[7] This result means that the energy gap of a bilayer graphene is zero, while the interlayer atomic interactions are neglected. E_g is also vanishing for a zero magnetic field [Fig. 1(c)]. As a result, the nonvanishing energy gap of a bilayer graphene is created by the cooperation of the interlayer atomic interactions and the magnetic field. It is reduced by the Zeeman effect (crosses). The Zeeman split-

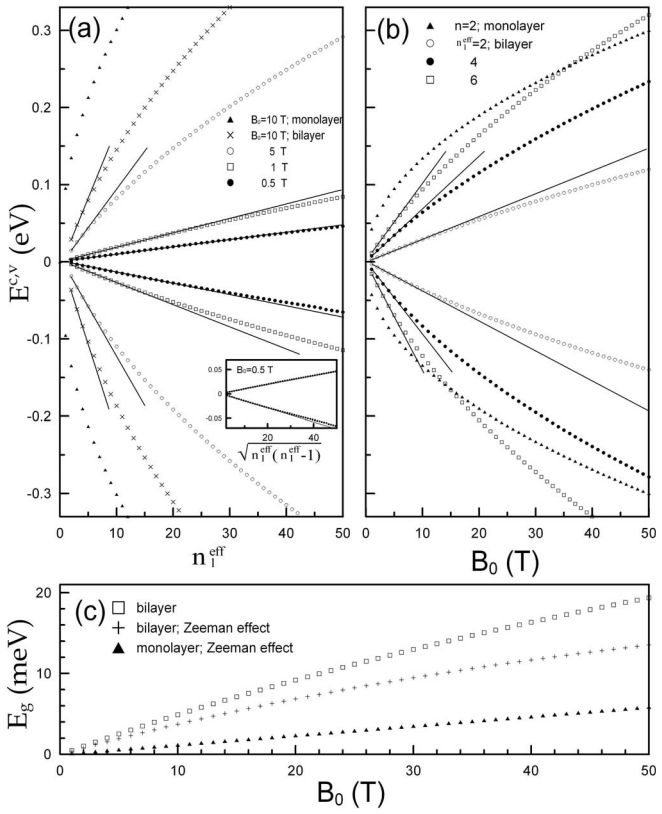

FIG. 6. The dependence of the very low Landau-level energy on (a) n_1^{eff} at different B_0's; (b) B_0 at different n_1^{eff}'s. The inset of (a) shows the dependence on $\sqrt{n_1^{eff}(n_1^{eff}-1)}$. (c) The B_0-dependent energy gap with or without the Zeeman splitting. Those of a monolayer graphene are also shown for comparison.

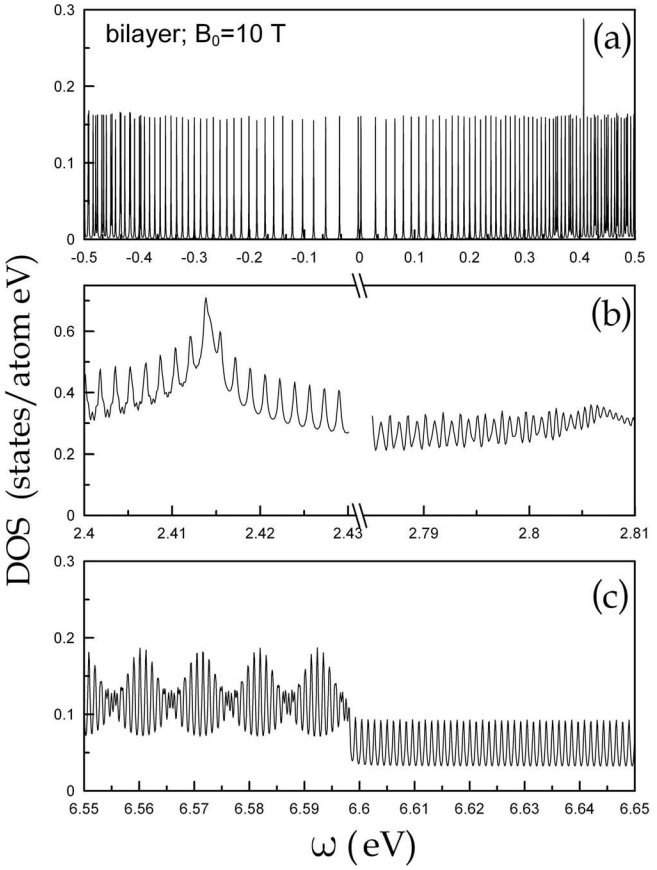

FIG. 7. Density of states of a bilayer graphene for $B_0=10$ T at (a) low, (b) moderate, and (c) high energies.

ting energy is $E_z=g\sigma B_0\pi/m^*\Phi_0$,[55] where $g=2$, $\sigma=\pm 1/2$, and m^* is the bare electron mass. Particularly, the energy gap of a monolayer graphene is purely caused by the Zeeman effect (solid triangles).

Density of states, which is closely related to the main characteristics of the LLs, is defined as

$$D(\omega)=\sum_{\sigma,h=c,v}\int_{1stBZ}\frac{dk_xdk_y}{4\pi^3}\frac{\Gamma}{[\omega-E^h(k_x,k_y)]^2+\Gamma^2}, \quad (17)$$

where the phenomenological broadening parameter is $\Gamma=0.5$ meV. $D(\omega)$ exhibits a lot of delta-function-like symmetric peaks at low energy, as shown in Fig. 7(a). These pronounced peaks originate from the first group of the dispersionless LLs, and their heights correspond to the fourfold degeneracy. The interlayer atomic interactions make them asymmetric about the Fermi level. The distribution of peaks is nonuniform owing to the unequally spaced Landau levels. The nonuniformity is strengthened by the advent of the second group of LLs at $E^c>\gamma_1+\gamma_6$ or $E^v<-\gamma_1+\gamma_6$. The height and the number of peaks become largest at moderate energy, as shown in Fig. 7(b). This result directly reflects the highest density of states at $B_0=0$.[18] $D(\omega)$ will decrease with the further increase of frequency. The lowest peak height occurs at $E^c\gtrsim(\sqrt{36\gamma_0^2-48\gamma_0\gamma_4+12\gamma_1^2}-\gamma_1-3\gamma_3+\gamma_6)/2$ [Fig. 7(c)], since there are only the second group of the doubly degenerate LLs. Density of states is associated with the available channels of optical excitations. The predicted features could be verified by the magneto-optical absorption spectroscopy.

The calculated results are similar to those done by the effective-mass approximation [25,26] only at very low energy $|E^{c,v}|\leqslant 50$ meV. The similarities include the dominant contributions from the B atoms on two layers, the oscillation modes of the carrier distributions, and the dependence of the Landau-level energy on quantum number and field strength. However, the tight-binding model and effective-mass approximation obtain different Landau-level energies even for $|E^{c,v}|\leqslant 50$ meV. The latter, which neglects some interlayer atomic interactions $(\gamma_3,\gamma_4,\gamma_6)$, might not account for the energy gap and the quite low Landau-level energies. The A atoms make important contributions to the LLs of the first group for $|E^{c,v}|>0.1$ eV. The LLs of the second group emerge at $E^c\gtrsim\gamma_1+\gamma_6$ and $E^v\lesssim-\gamma_1+\gamma_6$. Their wave functions are dominated by the A atoms, but not by the B atoms. E_g is significantly affected by (γ_3,γ_4), as discussed earlier. The wave functions solved with great efficiency by diagonalizing the Hamiltonian band matrix are expected to be useful in studying other physical properties, e.g., optical and transport properties.

IV. CONCLUDING REMARKS

The π-electronic structure of a bilayer Bernal graphene is calculated by the Peierls tight-binding model. A different

strategy, which derives the Hamiltonian band matrix by rearranging the base functions, is developed to investigate the magnetoelectronic properties at magnetic field $B_0 < 50$ T. Wave functions and state energies are obtained quite efficiently; therefore, they could be further utilized to study other physical properties. The interlayer atomic interactions and field strength dominate the main characteristics of LLs. The predicted Landau-level energies and effective quantum numbers can be examined by the experimental measurements on optical excitations and transport properties.

A uniform perpendicular magnetic field produces many dispersionless LLs at low and high energies, and some oscillatory LLs at moderate energy. State degeneracy of the low LLs is two times as much as that of the high LLs. The interlayer atomic interactions lead to two groups of LLs, more low LLs, the asymmetric LLs about the Fermi level, and change of level spacing. Two sets of effective quantum numbers are required to characterize the first and second groups of LLs. n_1^{eff} and n_2^{eff} are, respectively, associated with the B and A atoms. Which range of energy they emerge at depends on the specific interlayer atomic hoppings. Since (n_1^{eff}, n_2^{eff}) are determined by the strongest oscillation modes of the dominant carrier densities, they stand for the spatial symmetry configuration. Whether (n_1^{eff}, n_2^{eff}) satisfy the specific selection rule during the excitation processes is worthy of detailed research. The magneto-optical absorption spectra are under current investigations. The dependence of the quite low Landau-level energies on B_0 and n_1^{eff} is approximately linear. Energy gap is opened by the interlayer atomic interaction and magnetic field. E_g grows with the increase of field strength, while it is reduced by the Zeeman effect. In addition, the energy gap of a monolayer graphene purely comes from the Zeeman splitting. The main features of magnetoelectronic structures are directly reflected in the density of states.

*mflin@mail.ncku.edu.tw

[1] M. S. Dresselhaus and G. Dresselhaus, Adv. Phys. **30**, 139 (1981).
[2] D. E. Soule, Phys. Rev. **112**, 698 (1958).
[3] J. K. Galt, W. A. Yager, and H. W. Dail, Jr., Phys. Rev. **103**, 1586 (1956).
[4] T. Matsui, H. Kambara, Y. Niimi, K. Tagami, M. Tsukada, and H. Fukuyama, Phys. Rev. Lett. **94**, 226403 (2005).
[5] G. Li and E. Y. Andrei, Nat. Phys. **3**, 623 (2007).
[6] P. R. Wallace, Phys. Rev. **71**, 622 (1947).
[7] J. W. McClure, Phys. Rev. **104**, 666 (1956).
[8] J. C. Charlier, J.-P. Michenaud, and X. Gonze, Phys. Rev. B **46**, 4531 (1992).
[9] J. C. Charlier, J.-P. Michenaud, X. Gonze, and J.-P. Vigneron, Phys. Rev. B **44**, 13237 (1991).
[10] F. L. Shyu and M. F. Lin, J. Phys. Soc. Jpn. **69**, 3781 (2000).
[11] C. P. Chang, C. L. Lu, F. L. Shyu, R. B. Chen, Y. C. Huang, and M. F. Lin, Carbon **43**, 1424 (2005).
[12] K. S. Novoselov, A. K. Geim, S. V. Morozov, D. Jiang, Y. Zhang, S. V. Dubonos, I. V. Grigorieva, and A. A. Firsov, Science **306**, 666 (2004).
[13] K. S. Novoselov, A. K. Geim, S. V. Morozov, D. Jiang, M. I. Katsnelson, I. V. Grigorieva, S. V. Dubonos, and A. A. Firsov, Nature (London) **438**, 197 (2005).
[14] C. Berger, Z. M. Song, T. B. Li, X. B. Li, A. Y. Ogbazghi, R. Feng, Z. T. Dai, A. N. Marchenkov, E. H. Conrad, P. N. First, and W. A. de Heer, J. Phys. Chem. B **108**, 19912 (2004).
[15] C. Berger, Z. Song, X. Li, X. Wu, N. Brown, C. Naud, D. Mayou, T. Li, J. Hass, A. N. Marchenkov, E. H. Conrad, P. N. First, and W. A. de Heer, Science **312**, 1191 (2006).
[16] Y. Zheng and T. Ando, Phys. Rev. B **65**, 245420 (2002).
[17] E. McCann, Phys. Rev. B **74**, 161403(R) (2006).
[18] C. L. Lu, C. P. Chang, Y. C. Huang, J. M. Lu, C. C. Hwang, and M. F. Lin, J. Phys.: Condens. Matter **18**, 5849 (2006).
[19] F. Guinea, A. H. Castro Neto, and N. M. R. Peres, Phys. Rev. B **73**, 245426 (2006).
[20] E. McCann, K. Kechedzhi, V. I. Falko, H. Suzuura, T. Ando, and B. L. Altshuler, Phys. Rev. Lett. **97**, 146805 (2006).
[21] B. Partoens and F. M. Peeters, Phys. Rev. B **74**, 075404 (2006).
[22] M. Koshino and T. Ando, Phys. Rev. B **76**, 085425 (2007).
[23] C. L. Lu, C. P. Chang, J. H. Ho, C. C. Tsai, and M. F. Lin, Physica E (Amsterdam) **32**, 585 (2006).
[24] J. H. Ho, Y. H. Lai, S. J. Tsai, J. S. Hwang, C. P. Chang, and M. F. Lin, J. Phys. Soc. Jpn. **75**, 114703 (2006).
[25] E. McCann and V. I. Fal'ko, Phys. Rev. Lett. **96**, 086805 (2006).
[26] J. M. Pereira, F. M. Peeters, and P. Vasilopoulos, Phys. Rev. B **76**, 115419 (2007).
[27] N. Nemec and G. Cuniberti, Phys. Rev. B **75**, 201404(R) (2007).
[28] J. H. Ho, Y. H. Lai, Y. H. Chiu, and M. F. Lin, arXiv:0706.0078v1 (unpublished).
[29] J. H. Ho, Y. H. Lai, Y. H. Chiu, and M. F. Lin, Nanotechnology **19**, 035712 (2008).
[30] Y. H. Chiu, Y. H. Lai, J. H. Ho, D. S. Chuu, and M. F. Lin, Phys. Rev. B **77**, 045407 (2008).
[31] E. V. Castro, K. S. Novoselov, S. V. Morozov, N. M. R. Peres, J. M. B. Lopes dos Santos, J. Nilsson, F. Guinea, A. K. Geim, and A. H. Castro Neto, Phys. Rev. Lett. **99**, 216802 (2007).
[32] Y. Zhang, Y. W. Tan, H. L. Stormer, and P. Kim, Nature (London) **438**, 201 (2005).
[33] K. S. Novoselov, Z. Jiang, Y. Zhang, S. V. Morozov, H. L. Stormer, U. Zeitler, J. C. Maan, G. S. Boebinger, P. Kim, and A. K. Geim, Science **315**, 1379 (2007).
[34] K. S. Novoselov, E. McCann, S. V. Morozov, V. I. Fal'ko, M. I. Katsnelson, U. Zeitler, D. Jiang, F. Schedin, and A. K. Geim, Nat. Phys. **2**, 177 (2006).
[35] V. P. Gusynin and S. G. Sharapov, Phys. Rev. B **73**, 245411 (2006).
[36] V. P. Gusynin, V. A. Miransky, S. G. Sharapov, and I. A. Shovkovy, Phys. Rev. B **74**, 195429 (2006).
[37] M. Koshino and T. Ando, Phys. Rev. B **73**, 245403 (2006).
[38] J. Nilsson, A. H. Castro Neto, F. Guinea, and N. M. R. Peres, Phys. Rev. Lett. **97**, 266801 (2006).
[39] N. M. R. Peres, F. Guinea, and A. H. Castro Neto, Phys. Rev. B **73**, 125411 (2006).

[40] M. L. Sadowski, G. Martinez, M. Potemski, C. Berger, and W. A. de Heer, Phys. Rev. Lett. **97**, 266405 (2006).
[41] D. S. L. Abergel and V. I. Fal'ko, Phys. Rev. B **75**, 155430 (2007).
[42] R. S. Deacon, K.-C. Chuang, R. J. Nicholas, K. S. Novoselov, and A. K. Geim, Phys. Rev. B **76**, 081406(R) (2007).
[43] D. S. L. Abergel, A. Russell, and Vladimir I. Fal'ko, Appl. Phys. Lett. **91**, 063125 (2007).
[44] C. L. Lu, C. P. Chang, Y. C. Huang, R. B. Chen, and M. L. Lin, Phys. Rev. B **73**, 144427 (2006).
[45] C. L. Lu, H. L. Lin, C. C. Hwang, J. Wang, C. P. Chang, and M. F. Lin, Appl. Phys. Lett. **89**, 221910 (2006).
[46] O. L. Berman, Y. E. Lozovik, and G. Gumbs, arXiv:0706.0244 (unpublished).
[47] X.-F. Wang and T. Chakraborty, Phys. Rev. B **75**, 041404(R) (2007).
[48] X.-F. Wang and T. Chakraborty, Phys. Rev. B **75**, 033408 (2007).
[49] J. H. Ho, C. P. Chang, and M. F. Lin, Phys. Lett. A **352**, 446 (2006).
[50] J. H. Ho, C. P. Chang, R. B. Chen, and M. F. Lin, Phys. Lett. A **357**, 401 (2006).
[51] J. H. Ho, C. L. Lu, C. C. Hwang, C. P. Chang, and M. F. Lin, Phys. Rev. B **74**, 085406 (2006).
[52] M. F. Lin and F. L. Shyu, J. Phys. Soc. Jpn. **69**, 609 (2000).
[53] N. M. R. Peres, F. Guinea, and A. H. Castro Neto, Phys. Rev. B **72**, 174406 (2005).
[54] N. M. R. Peres, M. A. N. Araujo, and D. Bozi, Phys. Rev. B **70**, 195122 (2004).
[55] M. F. Lin and Kenneth W.-K. Shung, Phys. Rev. B **52**, 8423 (1995).